Enhanced photoelectrochemical hydrogen production efficiency of MoS2-Si heterojunction.

ALARAWI, A., RAMALINGAM, V., FU, H.-C., VARADHAN, P., YANG, R. and HE, J.-H.

2019

Research Article | Vol. 27, No. 8 | 15 Apr 2019 | OPTICS EXPRESS A352
Optics EXPRESS

Enhanced photoelectrochemical hydrogen production efficiency of MoS_2-Si heterojunction

ABEER ALARAWI,[1,4] VINOTH RAMALINGAM,[2,4] HUI-CHUN FU,[2] PURUSHOTHAMAN VARADHAN,[2] RUSEN YANG,[3] AND JR-HAU HE[2,*]

[1]*Material Science and Engineering (MSE) Division, King Abdullah University of Science & Technology (KAUST), Thuwal 23955-6900, Saudi Arabia*
[2]*Computer, Electrical, and Mathematical Sciences and Engineering (CEMSE) Division, King Abdullah University of Science & Technology (KAUST), Thuwal 23955-6900, Saudi Arabia*
[3]*School of Advanced Materials and Nanotechnology, Xidian University, Xi'an 710126, China*
[4]*Equal contribution*
[*]*jrhau.he@kaust.edu.sa*

Abstract: Photoelectrochemical water splitting is one of the viable approaches to produce clean hydrogen energy from water. Herein, we report MoS_2/Si-heterojunction (HJ) photocathode for PEC H_2 production. The MoS_2/Si-HJ photocathode exhibits exceptional PEC H_2 production performance with a maximum photocurrent density of 36.33 mA/cm^2, open circuit potential of 0.5 V *vs*. RHE and achieves improved long-term stability up to 10 h of reaction time. The photocurrent density achieved by MoS_2/Si-HJ photocathode is significantly higher than most of the MoS_2 coupled Si-based photocathodes reported elsewhere, indicating excellent PEC H_2 production performance.

1. Introduction

Solar-driven water splitting is one of the most promising approaches to utilize renewable energy to produce clean H_2 fuel [1,2]. The water splitting method can be categorized into two approaches which include electrochemical and solar-driven photoelectrochemical (PEC) H_2 production [3-6]. In general, PEC cell consists of two essential components i) photo-absorbing semiconductor to generate electron-hole pairs upon light illumination and ii) co-catalyst that facilitates charge transfer from semiconductor to the electrolyte and thereby induce the H_2 production process [7]. Among the wide range of light absorber materials, Si-based photocathodes have been widely adopted because of its low cost in the conventional solar industry [8,9]. Moreover, many theoretical studies have been illustrated that Si with the appropriate band-gap can perfectly align with the water oxidation–reduction potential levels [10].

In the PEC systems, *p*-type Si has been widely used as a photocathode for PEC H_2 production due to its downward band-bending in electrolyte, inexpensive and suitable band gap (~1.1 eV) to absorb solar light effectively. However, *p*-Si/H_2O junction causes an intrinsically low open-circuit voltage (V_{oc}), which greatly hampers the solar to H_2 conversion efficiency in PEC [9]. In contrast, replacing *p*-Si/electrolyte junction with a built-in *p*-*n* junction by adding an n^+-layer to the *p*-Si can boost the photovoltage [11]. For example, Lewis demonstrated that the onset potential could be improved to about 0.56 V when Pt is used as a co-catalyst, and *p*-Si is used that features a high level of n^+ surface doping [11]. This is because of the n^+-layer provides a built-in depletion region at the semiconductor-liquid junction [11]. Therefore, adding p^+-Si layer on the back of the n^+-*p* Si junction helps to facilitate the majority carrier collection, improving the device fill factor (FF) and overall performance [12].

#349934 https://doi.org/10.1364/OE.27.00A352
Journal © 2019 Received 2 Nov 2018; revised 11 Feb 2019; accepted 11 Feb 2019; published 18 Mar 2019

Optics EXPRESS

Platinum and other noble metals are the best-known electrocatalysts for hydrogen evolution reaction (HER), but the high cost and scarcity have significantly hindered their large-scale commercial usage [13,14]. Consequently, intensive research is devoted to exploring a new catalyst that possesses characteristics such as earth-abundant, inexpensive, and non-toxic and has a highly efficient catalytic performance towards HER. For example, metal alloys [15], chalcogenides [16], nitrides [17], phosphides [18], borides [19], transition metal dichalcogenides (TMDs) [20], perovskites [21], and carbides [22]. In fact, most of these new materials have only been utilized as standalone electrocatalysts, and few of them have been integrated with photocathodes for PEC H_2 production [23]. Furthermore, the appearance of interfacial defect states causes charge recombination sites due to the unappropriated band alignment of the light absorber/co-catalyst/electrolyte bands [24]. Also, there are fabrication issues related to control the morphology, thickness, and uniform deposition when using the direct synthesis of co-catalyst on the light absorbing substrate [25]. Molybdenum disulfide (MoS_2) as a co-catalyst has been widely integrated with Si photocathodes due to its electrochemical stability in the acidic environment, excellent HER activity, the direct controllable synthesis method, and favorable band-gap alignment with Si [26].

Herein, we demonstrate MoS_2/Si-HJ as an efficient photocathode for PEC H_2 production. The MoS_2/Si-HJ photocathode shows an ability to address the shortcoming of each component. We have achieved a half cell solar-to-hydrogen (STH) conversion efficiency of 5.57% under AM 1.5G illumination with a maximum photocurrent density of 36.33 mA/cm^2 and an onset potential of 0.5 V *vs*. RHE. Besides, the electrochemical impedance spectroscopy (EIS) elucidates that the integration of MoS_2 significantly reduced the charge transfer resistance and thereby enhanced the PEC H_2 production performance of MoS_2/Si-HJ photocathode. Accordingly, the integration of Si (excellent light harvesting) and MoS_2 (HER catalytic ability, and chemical protection) results in fabricating of an earth-abundant catalyst coupled photocathode that has an efficient and stable PEC H_2 production characteristics.

2. Experimental details

2.1 Synthesis of MoS_2

The thermal annealing method was used for the synthesis of MoS_2 [27]. The different concentrations of ammonium tetrathiomolybdate (0.5 to 1.5 M) was prepared in dimethylformamide (DMF) solution and subsequently ultra-sonicated for 30 min [28]. Then, the prepared precursor solution was spin coated (500 rpm for 30 s and then 1500 rpm for 45 s) on a fluorine-doped tin oxide (FTO) substrates and heated at 80 °C for 20 min in a vacuum oven. Afterward, the spin-coated MoS_2 film was transferred into a tube furnace and annealed at 450 °C for one h under Ar: H_2 (8:2) atmosphere to obtain MoS_2 thin film [28]. Importantly, H_2 gas plays a critical role to avoid creating MoO_3 during the growth process and improves the MoS_2 film quality. Equation (1) shows the thermal decomposition reaction involved for synthesis the MoS_2 from the initial precursor [28].

$$(NH_4)_2MoS_4 + H_2 \rightarrow 2NH_3 + 2H_2S + MoS_2 \quad (1)$$

2.2 Fabrication of MoS_2/Si-HJ photocathode

The photocathode includes several components. Firstly, *n*-type layers of (100) Si wafer with a thickness of 150 μm contains a dopant concentration of 5×10^{15} cm^{-3} that were fabricated on both sides of the cell by using an electrodeless chemical etching process [Solution of potassium hydroxide (KOH, 45 vol. %) and isopropyl alcohol (IPA)] to create a micro-pyramidal surface structure. Secondly, an emitter layer includes a 300 nm of p^+-Si with a dopant concentration of 9×10^{19} cm^{-3} which is formed by utilizing the thermal diffusion of BCl_3. Thirdly, the back surface field layer contains a 300 nm of n^+-Si with the dopant concentration of 3×10^{20} cm^{-3} that is fabricated by the thermal diffusion process of $POCl_4$.

By utilizing the techniques of atomic layer deposition and plasma-enhanced chemical vapor deposition, the 7 nm of Al_2O_3 and 50 nm of Si_3N_4 were deposited on the top of the emitter layer, respectively. Finally, both Al_2O_3 and Si_3N_4 layers were etched by HF, and then the photolithography and lift-off processes were applied to both materials, to deposit 300 nm of Ag on the top side of the cell. Furthermore, the p^+-layer side function is to harvest the light (light harvesting layer), due to its nearest location to the interface of the p^+-n junction position. Before MoS_2 deposition, Si cell was treated with buffer oxide etchant (BOE) to remove the native oxide layer followed by O_2 plasma for 3 min to make the hydrophilic Si surface for the better integration of MoS_2 precursor with Si photocathode. MoS_2 film on Si photocathode was prepared by drop-casting MoS_2 precursor solution on the n^+ side of Si and subsequently thermally annealed as described in MoS_2 synthesis (section 2.1).

For packing MoS_2/Si-HJ photocathode, Ga-In eutectic alloy (Sigma-Aldrich) was deposited on the electrode to make an Ohmic contact. The photocathode was subsequently connected with a Cu wire using silver paste. Samples then were embedded in Epoxy (Hysol 11C), and the only part that was covered with MoS_2 was exposed to the electrolyte. Epoxy then was dried at 80 °C for 30 min. The sample areas were then measured through the ImageJ software before the PEC measurements.

2.3 Characterizations

Raman spectroscopy measurements were carried out using a micro-Raman spectrometer. The samples were excited with a visible light laser [wavelength (λ = 473 nm)]. An objective lens at 100x magnification was used to focus the excitation laser on the desired spot of the MoS_2 thin film. Photoluminescence (PL) spectra of MoS_2 film was obtained using a Lab RAM micro-PL spectrometer. X-ray photoelectron spectroscopy (XPS) studies were carried out in a Kratos Axis Supra DLD spectrometer equipped with a monochromatic Al Ka X-ray source (hν = 1486.6 eV) operating at 150 W, a multi-channel plate and delay line detector under a vacuum of ~10^{-9} m bar. X-ray diffraction patterns (XRD) were collected at room temperature using a Bruker D8 Advance powder diffractometer (German Bruker) equipped with a Lynx-Eye detector and a Cu source. We used a field-emission scanning electron microscope (FE-SEM, Magellan and FEI) to observe the surface morphology. The TEM instrument used for this study was a probe Cs-corrected FEI-ST Titan 80–300 kV (ST) microscope. The high angle annular dark field-scanning electron microscopy (HAADF-STEM) were obtained using Titan Themis-Z TEM (TFS) at an operating voltage of 300 kV.

2.4 Electrochemical and photoelectrochemical (PEC) measurements

We evaluated the HER activity of the MoS_2 thin film at 25 °C in 0.5 M H_2SO_4 electrolyte using a standard three-electrode system, consists a MoS_2 electrode as the working electrode, Pt wire as the counter electrode, and Ag/AgCl (1 M KCl) as the reference electrode. All electrode potentials were converted with respect to RHE scale, according to Eq. (2). Also, all the HER curves were iR corrected to reflect the intrinsic behaviors of the catalysts.

$$E_{(RHE)} = E_{Ag/AgCl} + 0.197V \quad (2)$$

The electrochemical impedance spectroscopy (EIS) of the samples were measured at a frequency changing from 200 KHz to 100 MHz. For PEC measurements, AM 1.5G illumination was achieved with a 150 W halogen-lamp-based solar simulator. The chronoamperometry measurement was carried out using a three-electrode cell under one sun illumination in 0.5 M H_2SO_4. The amount of H_2 gas evolved during PEC experiments was measured using an online gas chromatography instrument (Agilent Technologies, 7890B GC system equipped with TCD detector).

Optics EXPRESS

3. Results and discussion

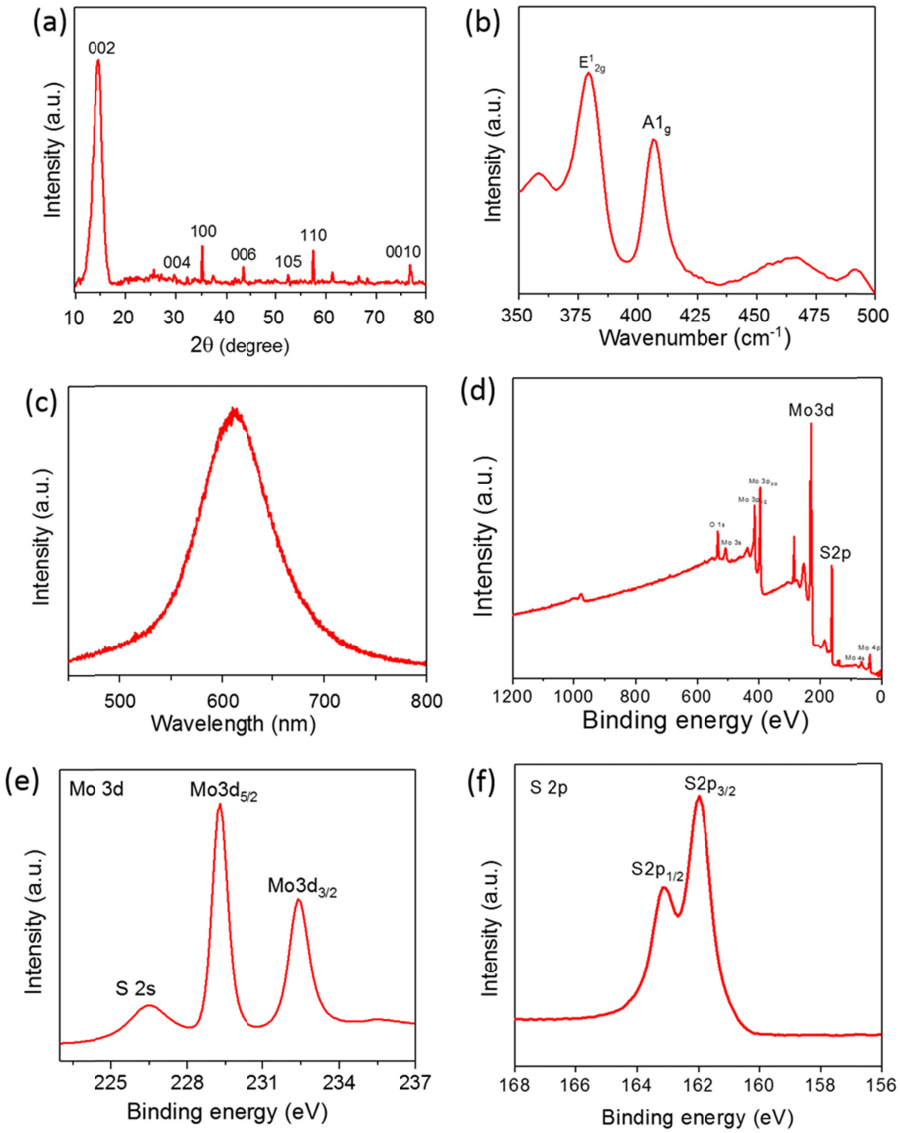

Fig. 1. (a) XRD patterns, (b) Raman spectra, (c) PL emission spectra, (d) XPS survey scan spectra, (e) High resolution Mo 3d XPS spectra and (f) High resolution S 2p XPS spectra of MoS_2 thin film.

Figure 1(a) shows the X-ray diffraction (XRD) patterns of as-synthesized 1M MoS_2 film on FTO substrate. A high intense peak noted at 2θ = ~14.6° corresponds to (002) plane of 2H-MoS_2 [29]. In addition, many smaller XRD peaks indicate the formation of polycrystalline multilayer MoS_2 film [30]. Figure 1(b) displays the Raman spectra of MoS_2 thin film. Two characteristic Raman peaks identified at ~379.3 cm^{-1} and 406.82 cm^{-1} are assigned to E^1_{2g} and A_{1g} mode of MoS_2. The peak positions confirmed the formation of MoS_2 after thermal annealing process [31,32]. Additionally, the 27.52 cm^{-1} separation between A^1_g and E^1_{2g} peaks indicates the presence of multilayer MoS_2 thin film [33]. The absence of vibrational peaks at 150 cm^{-1}, 219 cm^{-1}, and 327 cm^{-1} indicates that 2H-MoS_2 was obtained [34]. In order to investigate the semiconducting phase of the obtained MoS_2 film, we evaluated the

photoluminescence (PL) spectra as illustrated in Fig. 1(c). We observed that the thermal annealing of the MoS_2 precursor at 450 °C leads to a high-intensity PL feature at around 610 nm resulted from the 2H-MoS_2 excitons. The PL emission spectra for the multilayer film reflects the semiconductor phase of MoS_2 with a direct band gap of around 2 eV [35]. The peak at 610 nm reflects the energy of excitons which are radiatively recombining from the direct band gap. Moreover, it suggests that the observed PL arises from the intrinsic electronic properties of the multilayer MoS_2 and not from structural defects or chemical impurities [33]. The chemical state of MoS_2 film was further studied by X-ray photoelectron spectroscopy (XPS). The survey scan XPS spectra of 1M MoS_2 shows the existence of Mo and S elements, reveals the formation of MoS_2 thin film [Fig. 1(d)]. The high-resolution Mo3d XPS spectrum is depicted in Fig. 1(e). The Mo3d spectrum consists of binding energy peaks at around 229.3 eV and 232.4 eV, which correspond to $Mo3d_{5/2}$ and $Mo3d_{3/2}$ orbitals, respectively [29]. Additionally, a small binding energy peak centered at 226.8 eV is related to S2s. Likewise, high-resolution S2p XPS spectrum displays two peaks at 163.5 eV and 162.0 eV, which are assigned to $S2p_{1/2}$, and $S2p_{3/2}$ orbitals, respectively, that further indicates the presence of 2H-phase of MoS_2 [36]. Moreover, the Mo and S binding energies are in good agreement with previously reported values [37]. These results strongly suggest that the 2H-phase of MoS_2 is well preserved when the thermal annealing process is carried out at 450 °C.

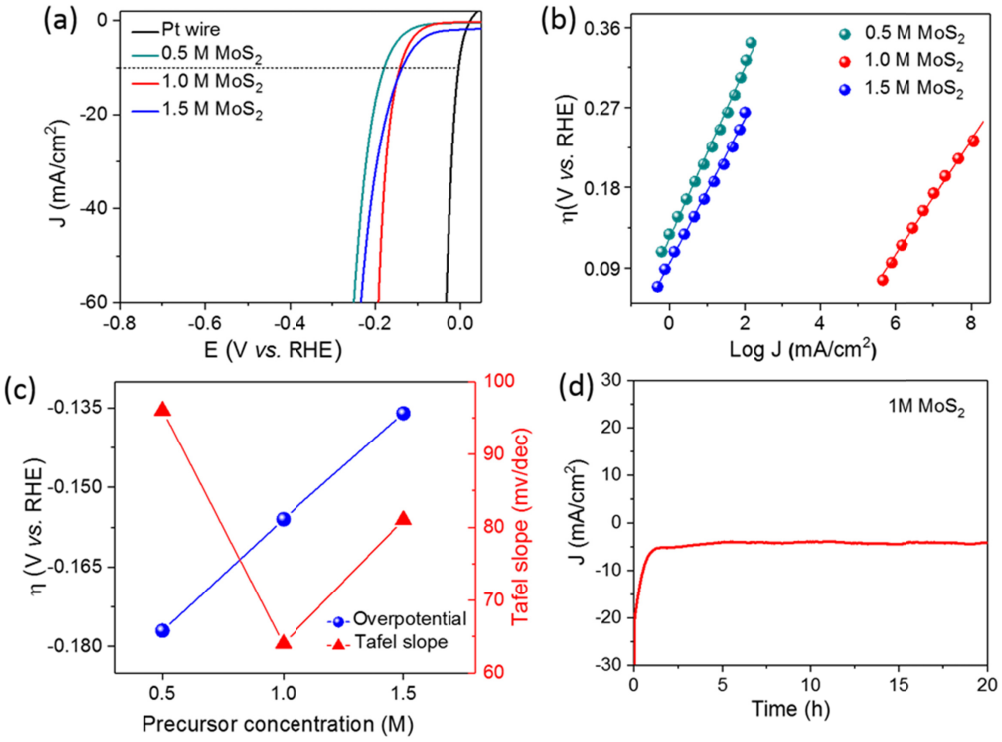

Fig. 2. (a) HER polarization curves of different precursor concentration derived MoS_2 (0.5, 1 and 1.5 M) and Pt wire in 0.5 M H_2SO_4 at a scan rate of 20 mV/s, (b) Corresponding Tafel plots, (c) Overpotential & Tafel values comparison and (d) Chronoamperometric test of 1M MoS_2 measured at a constant potential of 0.1 V vs. RHE.

Electrocatalytic HER activity of MoS_2 film was evaluated in 0.5 M H_2SO_4 electrolyte. Figure 2(a) displays the HER polarization curves of MoS_2 electrodes prepared using different precursor concentrations. The 0.5 M MoS_2, 1 M MoS_2 and 1.5 M MoS_2 catalysts exhibit an overpotentials of 0.177 V, 0.156 V and 0.136 V, respectively to reach 10 mA/cm^2 [Fig. 2(a)]. Interestingly, 1M MoS_2 shows excellent HER activity by offering low overpotential value at

high current density. For example, 1M MoS_2 exhibits an overpotential of 0.191 V to attain 60 mA/cm^2, which is smaller than the overpotential of MoS_2 prepared using 0.5M MoS_2 and 1.5M MoS_2 catalysts to achieve same current density. Based on the HER performance, MoS_2 catalyst prepared using 1M initial precursor solution was found to be the optimized HER catalyst. Moreover, the observed overpotential is almost similar to that of previously reported metallic MoS_2 nanosheets [38]. In order to gain more insights in reaction kinetics during HER, Tafel slope values were extracted from Tafel plots as shown in Fig. 2(b). The Tafel slope value of 1 M MoS_2 electrode is calculated to be 64 mV/decade, while 0.5 M and 1.5 M MoS_2 shows high Tafel values of 96 and 81 mV/decade, respectively. The smallest Tafel value offered by 1 M MoS_2 suggests that the mechanism of hydrogen adsorption/desorption is close to the Heyrovsky reaction regime (40 mV/decade) and the rate-limiting step here is the electrochemical desorption step [39]. Moreover, the Tafel value noted for 1 M MoS_2 quite agrees with previous reports of MoS_2 crystals, which range from 55 to 60 mV/ decade [40]. Overpotential and Tafel slope values comparison shows that 1 M MoS_2 is found to be optimized to achieve improved HER activity [Fig. 2(c)]. Stability is one of the most important factors used to evaluate the performance of a robust catalyst. Figure 2(d) shows chronoamperometry measurement that was used to analyze the long-term stability of the 1 M MoS_2 electrode at an overpotential of –0.1 V *vs.* RHE. The 1M MoS_2 is found to be stable up to 20h of continuous reactions with slight degradation in its performance, indicating excellent stability of MoS_2 in acidic environment.

A top view scanning electron microscopy (SEM) image of MoS_2 film reveals a continuous, ordered and compressed, featuring grains that cover the entire n^+ side of Si cell [Fig. 3(a)]. As shown in Fig. 3(b), SEM image of the front side of Si cell shows micro-pyramidal structure. Figure 3(c) shows the SEM image of MoS_2/Si-HJ PEC cell in which a conformal and smooth MoS_2 thin film catalyst is uniformly covered the Si micro-pyramidal surface with a thickness of ~1–1.5 μm. In addition, top view TEM shows that the thick flakes of MoS_2 with different sizes are covered the pyramidal Si surface [Fig. 3(c) inset]. Figures 3(d)-3(f) depicts the HR-TEM images of MoS_2/Si-HJ. The lattice fringes values (0.607 nm and 0.31 nm) correspond to MoS_2 noted in Figs. 3(d) and 3(e) indicates the successful integration of MoS_2 with Si. Also, the HR-TEM images confirm the nanosheets layer-by-layer growth mode on the faceted n^+-Si layer where the interface area appeared between the two materials. Figures 3(g) and 3(h) depict the HR-TEM image and its corresponding EDX mapping image at the interface between MoS_2 and Si. The HAADF-STEM image and its EDX mapping further reconfirm the integration of MoS_2 with Si. Furthermore, the mapping images confirm the existence of Mo, S and Si elements in MoS_2/Si-HJ [Figs. 3(i) and 3(l)].

Optics EXPRESS

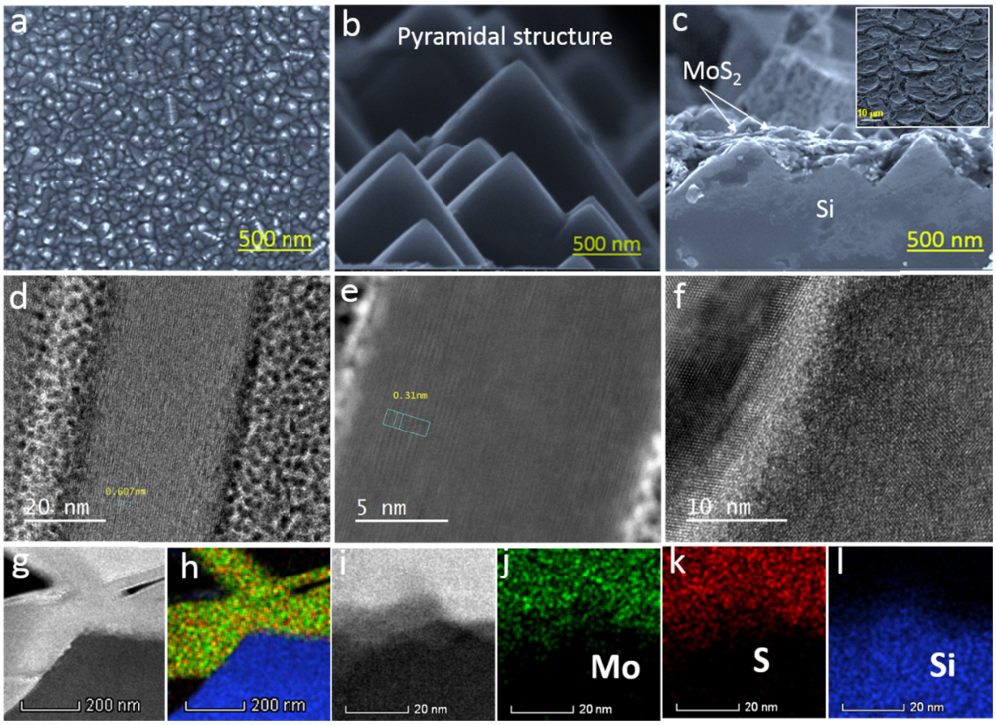

Fig. 3. (a) Top view SEM image of MoS_2 film, (b) SEM image of front surface of Si, (c) TEM image of MoS_2 coated Si (inset, top view TEM image of MoS_2/Si-HJ photocathode), (d-f) HR-TEM images of MoS_2/Si-HJ, (g, h) TEM image and its corresponding mapping and (i-l) HAADF-STEM mapping images of Mo, S and Si elements in MoS_2/Si-HJ.

The PEC H_2 production performance of the photocathode was evaluated in 0.5 M H_2SO_4 using a three-electrode assembly. Illumination of the working electrode was simulated by solar irradiance and calibrated to "one sun" based on the AM 1.5G standard [41]. Figure 4(a) illustrates the schematic structure of MoS_2/Si-HJ photocathode for PEC H_2 production. Figure 4(b) shows the LSV curves of bare Si and MoS_2/Si-HJ photocathodes under AM1.5 G illumination. As expected, bare Si photocathode exhibits poor PEC performance by offering large negative onset-potential value of –0.4 V *vs.* RHE and a maximum saturation photocurrent density value of about 26.2 mA/cm^2. Impressively, MoS_2/Si-HJ photocathode achieves an excellent PEC H_2 production performance with a positive onset potential of 0.5 V *vs*. RHE, which is similar to the V_{oc} of the Si-MP solar cell. Besides, MoS_2/Si-HJ photocathode has achieved a maximum photocurrent density of 36.33 mA cm^{-2} at 0 V *vs.* RHE, indicating an exceptional catalytic activity of MoS_2 as a co-catalyst in MoS_2/Si-HJ photocathode. Moreover, the achieved current density and onset potential values are higher than most of the literature reported on MoS_2/Si-based photocathodes (Table. 1). Because of the superior characteristics of the Si cell since it possesses the ability to minimize the charge reduction and improve the light harvesting. In addition, integration MoS_2 to this Si cell leads to reduce the charge transfer resistance and provide a complete corrosion protective layer thereby enhanced the solar to H_2 conversion performance. Most importantly, the high saturation current density values that can be obtained from the MoS_2/Si-HJ photocathode is close to the short circuit current density (J_{sc}) of Si MP solar cell, suggesting a minimal optical loss due to the efficient light-trapping properties of the Si MP structure. Figure 4(c) displays the MoS_2/Si-HJ photocathode response to ON/OFF light illumination. Besides, Fig. 4(d) demonstrates the stability measurement of MoS_2/Si-HJ photocathode in which the MoS_2/Si-HJ photocathode is found to be stable up to 600 min of reaction time. To explain the excellent

Optics EXPRESS

PEC H_2 production performance of the MoS_2/Si-HJ photocathode, we carried out electrochemical impedance spectroscopy (EIS). Figure 4(e) demonstrates the EIS spectra for bare Si cell and MoS_2/Si-HJ photocathodes measured under one sun illumination. Si photocathode without MoS_2 shows large charge transfer resistance, indicating poor interaction between electrolyte and Si surface. However, the MoS_2/Si-HJ photocathode has two distinguishable semicircles compared to that of bare Si cell [Fig. 4(e) inset]. The semicircles shape confirms the reduction of kinetics transport resistivity in MoS_2/Si-HJ photocathode. Furthermore, the semicircles proved the positive impact of the integration of the MoS_2 with Si, since more irreversible electrons can travel from Si to MoS_2 and thereby increasing its conductivity. Moreover, the unique Si cell structure increased the charge separation and decreased the recombination probability within the MoS_2/Si interface [42]. All of these factors played a significant role in increasing the MoS_2 electrons contribution for achieving efficient PEC H_2 production performance.

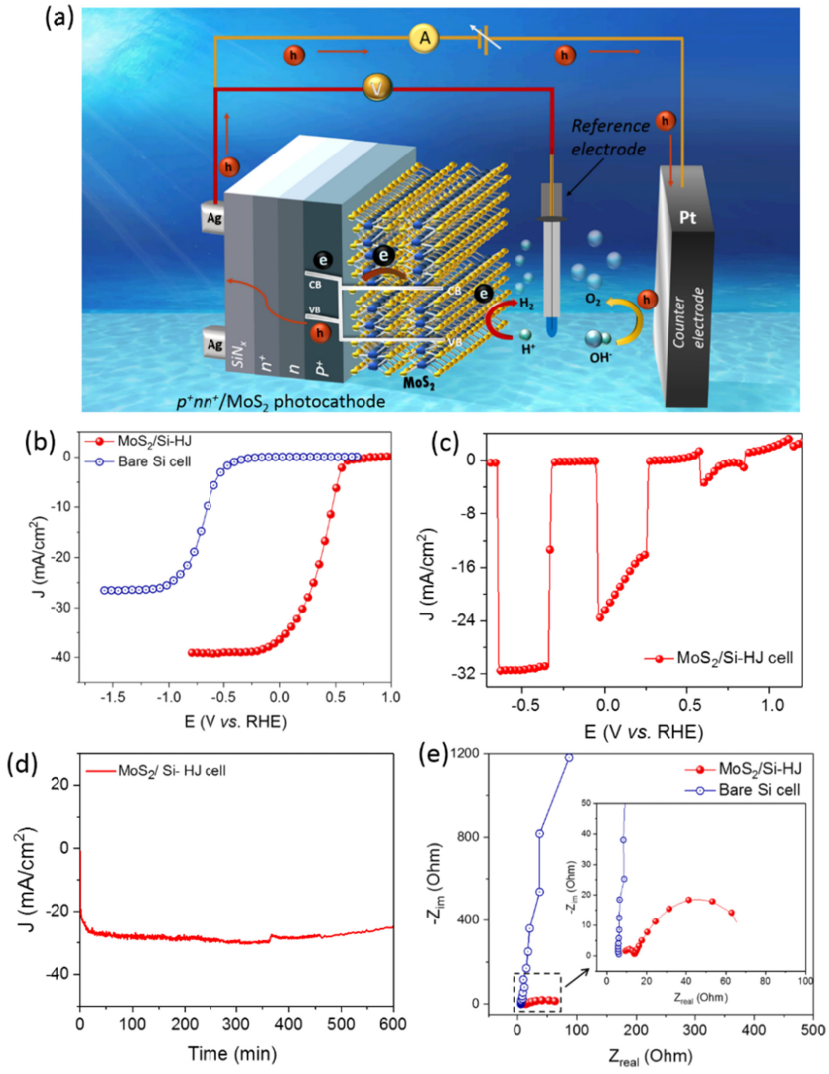

Fig. 4. (a) Schematic illustration of MoS_2 integrated Si photocathode for PEC H_2 production (b) LSV curve of bare Si cell and MoS_2/Si-HJ photocathode in 0.5 M H_2SO_4 at a scan rate of 20 mV/s upon AM 1.5G illumination, (c) MoS_2/Si-HJ photocathode response to ON/OFF

illumination, (d) Stability curve of MoS_2/Si-HJ photocathode in 0.5 M H_2SO_4 and (e) EIS spectra of bare Si cell and MoS_2/Si-HJ photocathode under AM 1.5G illumination.

Finally, the half-cell solar-to-hydrogen conversion efficiency (η_{STH}), which refers to the relationship between the input energy (solar irradiation) to the output energy (electric or chemical energy via hydrogen evolution subtracted from the input applied potential) has been calculated using the following Eq. (3) [41].

$$\eta_{STH}(\%) = \frac{V_{oc} \times FF \times J_{sc}}{P_{in}}(\%) \quad (3)$$

where J_{sc}, FF and V_{oc} represents the photocurrent density, fill factor and open-circuit potential of the PEC device [41]. Based on Eq. (3), the MoS_2 /Si-HJ photocathode achieves a half-cell η_{STH} of 5.5%. The amount of H_2 gas evolved by MoS_2/Si-HJ photocathode under light illumination was measured using an online gas chromatography instrument (Fig. 5). The H_2 gas produced by MoS_2/Si-HJ photocathode matches well with theoretically calculated H_2 value. The Faradaic efficiency of MoS_2/Si-HJ photocathode was estimated to be about 100%, suggesting the outstanding PEC H_2 production performance of MoS_2/Si-HJ photocathode.

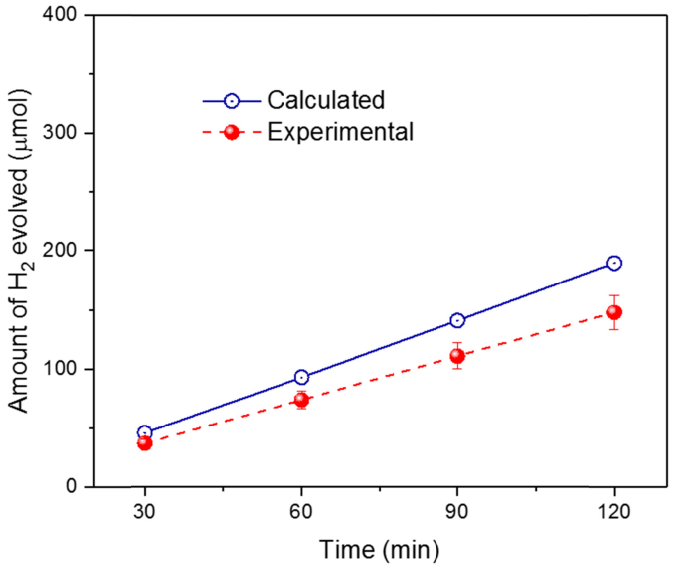

Fig. 5. Theoretically calculated and experimentally evolved amount of H_2 using MoS_2/Si-HJ photocathode under AM1.5G light illumination

Table 1. Comparison on the PEC H_2 production performance of MoS_2/Si-HJ photocathode with the reported MoS_2 integrated Si photocathodes.

Photocathode Structure	Electrolyte	Photocurrent Onset Potential (*V vs. RHE*)	Photocurrent Density (*mA/cm² at 0 V*)	Stability (h)	Ref.
MoS_2/n^+-n-p^+ Si	0.5 M H_2SO_4	+ 0.5	36.34	10	*This work*
MoS_2/n^+p Si	0.5 M H_2SO_4	–0.20 to - 0.10	17	100	[43]

Optics EXPRESS

$MoS_2/Al_2O_3/n^+p$-Si	0.5 M H_2SO_4	+ 0.35	34.5	40	[44]
1T-MoS_2/p-Si	0.5 M H_2SO_4	+ 0.25	17.6	3	[26]
MoS_x /Ti /n^+p-Si	1 M $HClO_4$	+ 0.33	16	1	[45]
MoS_2/TiO_2/Si NW	0.5 M H_2SO_4	+ 0.30	15	75	[46]
Si/a-$CoMoS_x$	Phosphate solution	+ 0.25	17.5	3	[47]
MoS_2 /p-Si in wafer scale	0.5 M H_2SO_4	- 0.79 V	24.6	10 000 Seconds	[48]
MoS_2 /Al_2O_3/n^+p-Si	1 M $HClO_4$	+ 0.4 V	35.6	120	[49]
Si nanowires/MoS_2	0.5 M H_2SO_4	+ 0.26 V	16.5	48	[50]

4. Conclusion

In conclusion, MoS_2/Si-HJ photocathode reported herein exhibited a maximum half-cell η_{STH} of 5.5% with a high photocurrent density of 36.33 mA/cm^2, an open circuit potential of 0.5 V *vs.* RHE, and stability up to 10 h of continuous reaction time. The EIS measurement demonstrated that the integration of MoS_2 significantly reduced the charge-transfer resistances across either the MoS_2/Si-HJ interface or the MoS_2/electrolyte interface and thereby significantly enhance the PEC H_2 production efficiency. The excellent PEC H_2 production performance of the integrated photocathode provides a promising alternative for non-noble metal co-catalysts toward solar-driven hydrogen production. Importantly, this will also lead to additional research and exploration to employ the semiconducting metal chalcogenides for PEC applications.

Funding

King Abdullah University of Science and Technology (KAUST) Office of Sponsored Research (OSR-2016-CRG5-3005), KAUST Sensor Initiative, KAUST Solar Center, KAUST Catalysis Center and KAUST baseline funding.

References

1. Y. Tachibana, L. Vayssieres, and J. R. Durrant, "Artificial photosynthesis for solar water-splitting," Nat. Photonics **6**(8), 511–518 (2012).
2. M. G. Walter, E. L. Warren, J. R. McKone, S. W. Boettcher, Q. Mi, E. A. Santori, and N. S. Lewis, "Solar water splitting cells," Chem. Rev. **110**(11), 6446–6473 (2010).
3. C.-H. Liao, C.-W. Huang, and J. C. S. Wu, "Hydrogen production from semiconductor-based photocatalysis via water splitting," Catalysts **2**(4), 490–516 (2012).
4. S. Y. Tee, K. Y. Win, W. S. Teo, L.-D. Koh, S. Liu, C. P. Teng, and M.-Y. Han, "Recent progress in energy-driven water splitting," Adv. Sci. (Weinh.) **4**(5), 1600337 (2017).
5. A. Alarawi, V. Ramalingam, and J.-H. He, "Recent advances in emerging single atom confined two-dimensional materials for water splitting applications," Mater. Today Energy **11**, 1–23 (2019).
6. Z. Cai, X. Bu, P. Wang, J. C. Ho, J. Yang, and X. Wang, "Recent advances on layered double hydroxide electrocatalysts for oxygen evolution reaction," J. Mater. Chem. A (2019).
7. C. Jiang, S. J. A. Moniz, A. Wang, T. Zhang, and J. Tang, "Photoelectrochemical devices for solar water splitting - materials and challenges," Chem. Soc. Rev. **46**(15), 4645–4660 (2017).
8. S. Y. Reece, J. A. Hamel, K. Sung, T. D. Jarvi, A. J. Esswein, J. J. H. Pijpers, and D. G. Nocera, "Wireless solar water splitting using silicon-based semiconductors and earth-abundant catalysts," Science **334**(6056), 645–648 (2011).
9. H.-P. Wang, K. Sun, S. Y. Noh, A. Kargar, M.-L. Tsai, M.-Y. Huang, D. Wang, and J.-H. He, "High-performance a-Si/c-Si heterojunction photoelectrodes for photoelectrochemical oxygen and hydrogen evolution," Nano Lett. **15**(5), 2817–2824 (2015).
10. Q. Ding, B. Song, P. Xu, and S. Jin, "Efficient electrocatalytic and photoelectrochemical hydrogen generation using MoS_2 and related compounds," Chem **1**(5), 699–726 (2016).

Optics EXPRESS

11. S. W. Boettcher, E. L. Warren, M. C. Putnam, E. A. Santori, D. Turner-Evans, M. D. Kelzenberg, M. G. Walter, J. R. McKone, B. S. Brunschwig, H. A. Atwater, and N. S. Lewis, "Photoelectrochemical hydrogen evolution using Si microwire arrays," J. Am. Chem. Soc. **133**(5), 1216–1219 (2011).
12. D. Bae, T. Pedersen, B. Seger, M. Malizia, A. Kuznetsov, O. Hansen, I. Chorkendorff, and P. C. K. Vesborg, "Back-illuminated Si photocathode: A combined experimental and theoretical study for photocatalytic hydrogen evolution," Energy Environ. Sci. **8**(2), 650–660 (2015).
13. N. S. Lewis and D. G. Nocera, "Powering the planet: chemical challenges in solar energy utilization," Proc. Natl. Acad. Sci. U.S.A. **103**(43), 15729–15735 (2006).
14. J. A. Turner, "Sustainable hydrogen production," Science **305**(5686), 972–974 (2004).
15. J. R. McKone, E. L. Warren, M. J. Bierman, S. W. Boettcher, B. S. Brunschwig, N. S. Lewis, and H. B. Gray, "Evaluation of Pt, Ni, and Ni–Mo electrocatalysts for hydrogen evolution on crystalline Si electrodes," Energy Environ. Sci. **4**(9), 3573–3583 (2011).
16. D. Voiry, M. Salehi, R. Silva, T. Fujita, M. Chen, T. Asefa, V. B. Shenoy, G. Eda, and M. Chhowalla, "Conducting MoS□ nanosheets as catalysts for hydrogen evolution reaction," Nano Lett. **13**(12), 6222–6227 (2013).
17. W.-F. Chen, K. Sasaki, C. Ma, A. I. Frenkel, N. Marinkovic, J. T. Muckerman, Y. Zhu, and R. R. Adzic, "Hydrogen-evolution catalysts based on non-noble metal nickel-molybdenum nitride nanosheets," Angew. Chem. Int. Ed. Engl. **51**(25), 6131–6135 (2012).
18. E. J. Popczun, J. R. McKone, C. G. Read, A. J. Biacchi, A. M. Wiltrout, N. S. Lewis, and R. E. Schaak, "Nanostructured nickel phosphide as an electrocatalyst for the hydrogen evolution reaction," J. Am. Chem. Soc. **135**(25), 9267–9270 (2013).
19. H. Vrubel and X. Hu, "Molybdenum boride and carbide catalyze hydrogen evolution in both acidic and basic solutions," Angew. Chem. Int. Ed. Engl. **51**(51), 12703–12706 (2012).
20. J. Yang and H. S. Shin, "Recent advances in layered transition metal dichalcogenides for hydrogen evolution reaction," J. Mater. Chem. A Mater. Energy Sustain. **2**(17), 5979–5985 (2014).
21. A. M. Al-Amri, B. Cheng, and J.-H. He, "Perovskite methylammonium lead trihalide heterostructures: progress and challenges," IEEE Trans. NanoTechnol. **18**, 1–12 (2019).
22. W. F. Chen, C. H. Wang, K. Sasaki, N. Marinkovic, W. Xu, J. T. Muckerman, Y. Zhu, and R. R. Adzic, "Highly active and durable nanostructured molybdenum carbide electrocatalysts for hydrogen production," Energy Environ. Sci. **6**(3), 943–951 (2013).
23. J. Willkomm, K. L. Orchard, A. Reynal, E. Pastor, J. R. Durrant, and E. Reisner, "Dye-sensitised semiconductors modified with molecular catalysts for light-driven H_2 production," Chem. Soc. Rev. **45**(1), 9–23 (2016).
24. K. O. Davis and W. V. Schoenfeld, "Engineered interfaces using surface and contact passivation in silicon solar cells," Electrochem. Soc. Interface **27**(1), 63–66 (2018).
25. J. R. McKone, N. S. Lewis, and H. B. Gray, "Will solar-driven water-splitting devices see the light of day," Chem. Mater. **26**(1), 407–414 (2014).
26. Q. Ding, F. Meng, C. R. English, M. Cabán-Acevedo, M. J. Shearer, D. Liang, A. S. Daniel, R. J. Hamers, and S. Jin, "Efficient photoelectrochemical hydrogen generation using heterostructures of Si and chemically exfoliated metallic MoS_2," J. Am. Chem. Soc. **136**(24), 8504–8507 (2014).
27. K.-K. Liu, W. Zhang, Y.-H. Lee, Y.-C. Lin, M.-T. Chang, C.-Y. Su, C.-S. Chang, H. Li, Y. Shi, H. Zhang, C.-S. Lai, and L.-J. Li, "Growth of large-area and highly crystalline MoS_2 thin layers on insulating substrates," Nano Lett. **12**(3), 1538–1544 (2012).
28. F. Qi, P. Li, Y. Chen, B. Zheng, X. Liu, F. Lan, Z. Lai, Y. Xu, J. Liu, J. Zhou, J. He, and W. Zhang, "Effect of hydrogen on the growth of MoS_2 thin layers by thermal decomposition method," Vacuum **119**, 204–208 (2015).
29. G. Pagona, C. Bittencourt, R. Arenal, and N. Tagmatarchis, "Exfoliated semiconducting pure 2H-MoS_2 and 2H-WS_2 assisted by chlorosulfonic acid," Chem. Commun. (Camb.) **51**(65), 12950–12953 (2015).
30. C. P. Veeramalai, F. Li, Y. Liu, Z. Xu, T. Guo, and T. W. Kim, "Enhanced field emission properties of molybdenum disulphide few layer nanosheets synthesized by hydrothermal method," Appl. Surf. Sci. **389**, 1017–1022 (2016).
31. C. Lee, H. Yan, L. E. Brus, T. F. Heinz, J. Hone, and S. Ryu, "Anomalous lattice vibrations of single- and few-layer MoS_2," ACS Nano **4**(5), 2695–2700 (2010).
32. J. L. Brito, M. Ilija, and P. Hernández, "Thermal and reductive decomposition of ammonium thiomolybdates," Thermochim. Acta **256**(2), 325–338 (1995).
33. K. F. Mak, C. Lee, J. Hone, J. Shan, and T. F. Heinz, "Atomically thin MoS□: a new direct-gap semiconductor," Phys. Rev. Lett. **105**(13), 136805 (2010).
34. M. A. Lukowski, A. S. Daniel, F. Meng, A. Forticaux, L. Li, and S. Jin, "Enhanced hydrogen evolution catalysis from chemically exfoliated metallic MoS_2 nanosheets," J. Am. Chem. Soc. **135**(28), 10274–10277 (2013).
35. G. Eda, H. Yamaguchi, D. Voiry, T. Fujita, M. Chen, and M. Chhowalla, "Photoluminescence from chemically exfoliated MoS_2," Nano Lett. **11**(12), 5111–5116 (2011).
36. Y. Shi, Y. Zhou, D.-R. Yang, W.-X. Xu, C. Wang, F.-B. Wang, J.-J. Xu, X.-H. Xia, and H.-Y. Chen, "Energy level engineering of MoS_2 by transition-metal doping for accelerating hydrogen evolution reaction," J. Am. Chem. Soc. **139**(43), 15479–15485 (2017).

Optics EXPRESS

37. M. A. Baker, R. Gilmore, C. Lenardi, and W. Gissler, "XPS investigation of preferential sputtering of s from MoS_2 and determination of mosx stoichiometry from Mo and S peak positions," Appl. Surf. Sci. **150**(1-4), 255–262 (1999).
38. J. Wang, N. Wang, Y. Guo, J. Yang, J. Wang, F. Wang, J. Sun, H. Xu, Z.-H. Liu, and R. Jiang, "Metallic-phase MoS_2 nanopetals with enhanced electrocatalytic activity for hydrogen evolution," ACS Sustain. Chem.& Eng. **6**(10), 13435–13442 (2018).
39. D. Kiriya, P. Lobaccaro, H. Y. Y. Nyein, P. Taheri, M. Hettick, H. Shiraki, C. M. Sutter-Fella, P. Zhao, W. Gao, R. Maboudian, J. W. Ager, and A. Javey, "General thermal texturization process of MoS_2 for efficient electrocatalytic hydrogen evolution reaction," Nano Lett. **16**(7), 4047–4053 (2016).
40. T. F. Jaramillo, K. P. Jørgensen, J. Bonde, J. H. Nielsen, S. Horch, and I. Chorkendorff, "Identification of active edge sites for electrochemical H_2 evolution from MoS_2 nanocatalysts," Science **317**(5834), 100–102 (2007).
41. Z. Chen, H. N. Dinh, and E. Miller, *Photoelectrochemical water splitting: Standards, experimental methods, and protocols* (Springer, 2013).
42. W. Ouyang, F. Teng, J.-H. He, and X. Fang, "Enhancing the photoelectric performance of photodetectors based on metal oxide semiconductors by charge-carrier engineering," Adv. Funct. Mater., 1807672 (2019).
43. J. D. Benck, S. C. Lee, K. D. Fong, J. Kibsgaard, R. Sinclair, and T. F. Jaramillo, "Designing active and stable silicon photocathodes for solar hydrogen production using molybdenum sulfide nanomaterials," Adv. Energy Mater. **4**(18), 1400739 (2014).
44. J. Zhou, S. Dai, W. Dong, X. Su, L. Fang, F. Zheng, X. Wang, and M. Shen, "Efficient and stable MoS_2 catalyst integrated on Si photocathodes by photoreduction and post-annealing for water splitting," Appl. Phys. Lett. **108**(21), 213905 (2016).
45. B. Seger, A. B. Laursen, P. C. K. Vesborg, T. Pedersen, O. Hansen, S. Dahl, and I. Chorkendorff, "Hydrogen production using a molybdenum sulfide catalyst on a titanium-protected $n(^{+})p^{-}$silicon photocathode," Angew. Chem. Int. Ed. Engl. **51**(36), 9128–9131 (2012).
46. L. Zhang, C. Liu, A. B. Wong, J. Resasco, and P. Yang, "MoS_2-wrapped silicon nanowires for photoelectrochemical water reduction," Nano Res. **8**(1), 281–287 (2015).
47. Y. Chen, P. D. Tran, P. Boix, Y. Ren, S. Y. Chiam, Z. Li, K. Fu, L. H. Wong, and J. Barber, "Silicon decorated with amorphous cobalt molybdenum sulfide catalyst as an efficient photocathode for solar hydrogen generation," ACS Nano **9**(4), 3829–3836 (2015).
48. K. C. Kwon, S. Choi, K. Hong, C. W. Moon, Y.-S. Shim, D. H. Kim, T. Kim, W. Sohn, J.-M. Jeon, C.-H. Lee, K. T. Nam, S. Han, S. Y. Kim, and H. W. Jang, "Wafer-scale transferable molybdenum disulfide thin-film catalysts for photoelectrochemical hydrogen production," Energy Environ. Sci. **9**(7), 2240–2248 (2016).
49. R. Fan, J. Mao, Z. Yin, J. Jie, W. Dong, L. Fang, F. Zheng, and M. Shen, "Efficient and stable silicon photocathodes coated with vertically standing nano-MoS_2 films for solar hydrogen production," ACS Appl. Mater. Interfaces **9**(7), 6123–6129 (2017).
50. D. Hu, J. Xiang, Q. Zhou, S. Su, Z. Zhang, X. Wang, M. Jin, L. Nian, R. Nözel, G. Zhou, Z. Zhang, and J. Liu, "One-step chemical vapor deposition of MoS_2 nanosheets on SiNWs as photocathodes for efficient and stable solar-driven hydrogen production," Nanoscale **10**(7), 3518–3525 (2018).